

Ultra-selective high-flux membranes from directly synthesized zeolite nanosheets

Mi Young Jeon^{1*}, Donghun Kim^{1*}, Prashant Kumar^{1*}, Pyung Soo Lee^{1*†}, Neel Rangnekar¹, Peng Bai^{1,2}, Meera Shete¹, Bahman Elyassi¹, Han Seung Lee¹, Katabathini Narasimharao³, Sulaiman Nasir Basahel³, Shaeel Al-Thabaiti³, Wenqian Xu⁴, Hong Je Cho⁵, Evgenii O. Fetisov², Raghuram Thyagarajan², Robert F. DeJaco¹, Wei Fan⁵, K. Andre Mkhoyan¹, J. Ilja Siepmann² & Michael Tsapatsis¹

A zeolite with structure type MFI^{1,2} is an aluminosilicate or silicate material that has a three-dimensionally connected pore network, which enables molecular recognition in the size range 0.5–0.6 nm. These micropore dimensions are relevant for many valuable chemical intermediates, and therefore MFI-type zeolites are widely used in the chemical industry as selective catalysts or adsorbents^{3–5}. As with all zeolites, strategies to tailor them for specific applications include controlling their crystal size and shape^{5–8}. Nanometre-thick MFI crystals (nanosheets) have been introduced in pillared⁹ and self-pillared (intergrown)¹⁰ architectures, offering improved mass-transfer characteristics for certain adsorption and catalysis applications^{11–14}. Moreover, single (non-intergrown and non-layered) nanosheets have been used to prepare thin membranes^{15,16} that could be used to improve the energy efficiency of separation processes¹⁷. However, until now, single MFI nanosheets have been prepared using a multi-step approach based on the exfoliation of layered MFI^{9,15}, followed by centrifugation to remove non-exfoliated particles¹⁸. This top-down method is time-consuming, costly and low-yield and it produces fragmented nanosheets with submicrometre lateral dimensions. Alternatively, direct (bottom-up) synthesis could produce high-aspect-ratio zeolite nanosheets, with improved yield and at lower cost. Here we use a nanocrystal-seeded growth method triggered by a single rotational intergrowth to synthesize high-aspect-ratio MFI nanosheets with a thickness of 5 nanometres (2.5 unit cells). These high-aspect-ratio nanosheets allow the fabrication of thin and defect-free coatings that effectively cover porous substrates. These coatings can be intergrown to produce high-flux and ultra-selective MFI membranes that compare favourably with other MFI membranes prepared from existing MFI materials (such as exfoliated nanosheets or nanocrystals).

We achieved the bottom-up synthesis of MFI nanosheets by hydrothermal growth of MFI seeds approximately 30 nm in diameter (Fig. 1) in the presence of bis-1,5(triisopropyl ammonium) pentamethylene diiodide (hereafter denoted as dC5; see Extended Data Fig. 1a). The tetraethyl ammonium cation (TEA; see Extended Data Fig. 1e) is the most effective structure-directing agent (SDA) for MFI. Its dimers, like dC5 (the dimer with five methylene carbons connecting the two nitrogen atoms), are known to yield distinct crystal morphologies depending on the length of the nitrogen-bridging alkyl chains^{6,19}. dC5, in particular, can direct the formation of plate-like MFI^{6,20} with the thin crystal dimension along the *b* axis, a morphology that is considered favourable for membrane applications, owing to the presence of straight micropores along this direction²¹.

However, a bottom-up (not based on exfoliation) synthesis of single nanosheets has not been achieved until now owing to the formation

of orthogonal intergrowths (MFI twins). In fact, the propensity for twin formation in the presence of dC5 has been elegantly exploited to create MFI crystals with hierarchical porosity²⁰ (Extended Data Fig. 1b). Earlier, we suggested that the formation of MFI and other zeolite rotational intergrowths^{10,22} are preceded by the intergrowth of a related zeolite structure with different symmetry. In the case of MFI, the orthogonal intergrowth is probably caused by the incorporation of the higher-symmetry framework type MEL¹⁰ (Extended Data Fig. 1c). Insertion of MEL segments within MFI has been detected by electron microscopy²³, and it has been described from crystallography and crystal growth mechanism standpoints on the basis of the placement of silicate chains (called pentasil chains; see Extended Data Fig. 1d) along the common *c* axis of MFI and MEL²⁴. MFI is formed when the pentasil chains grow so that an inversion centre exists along the *a* axis, whereas MEL is formed when the pentasil chains relate by a mirror plane.

From the above arguments (made in ref. 24) regarding the arrangement of pentasil chains and our proposal that MEL domains trigger orthogonal intergrowths¹⁰, we hypothesized that the emergence of orthogonal intergrowths is favoured on flat, well developed, crystal facets on which MEL-forming pentasil chain arrangements can extend along the common *c* axis of MEL and MFI. Therefore, to avoid intergrowths, we investigated seeded growth with nanometre-sized seeds that do not have well defined facets and, therefore, cannot support orthogonal intergrowth at early stages of growth (see Extended Data Fig. 1f). Indeed, after extensive variation of synthesis conditions, we identified a synthesis window that produces zeolite nanosheets free of rotational intergrowths.

Figure 1a shows schematic illustrations and the corresponding transmission electron microscopy (TEM) images of seed crystals (depicted in red) and nanosheets (depicted in yellow) from different growth stages. For an extended time (typically 20–40 h), the MFI nanocrystal seeds grow slowly to acquire a near-cylindrical shape (depicted in Fig. 1b). Figure 1c shows a typical cylindrical nanocrystal grown to 140 nm in length with the corresponding electron diffraction pattern and also high-resolution TEM images along the three MFI axes of similar nanocrystals. In accordance with an earlier report⁶, we determined the long axis of the cylindrical crystals to be the *b* axis of MFI (see also Extended Data Fig. 2a–f). Examination of several crystals at this stage of growth does not yield any evidence of rotational intergrowth, and the lack thereof supports the underlying hypothesis of this work. In most crystals examined at this stage, owing to slight misorientation with respect to the remainder of the crystal, the original 30-nm seed can be made visible using dark-field TEM imaging (Extended Data Fig. 2g–i). This observation indicates that the cylindrical crystals evolve

¹Department of Chemical Engineering and Materials Science, University of Minnesota, Minneapolis, Minnesota 55455, USA. ²Department of Chemistry and Chemical Theory Center, University of Minnesota, Minneapolis, Minnesota 55455, USA. ³Department of Chemistry, Faculty of Science, King Abdulaziz University, Jeddah 21589, Saudi Arabia. ⁴X-ray Science Division, Advanced Photon Source, Argonne National Laboratory, Lemont, Illinois 60439, USA. ⁵Department of Chemical Engineering, University of Massachusetts Amherst, Amherst, Massachusetts 01003, USA. [†]Present address: Center for Membrane, Advanced Green Chemical Materials Division, Korea Research Institute of Chemical Technology (KRICT), Daejeon 34114, South Korea.

*These authors contributed equally to this work.

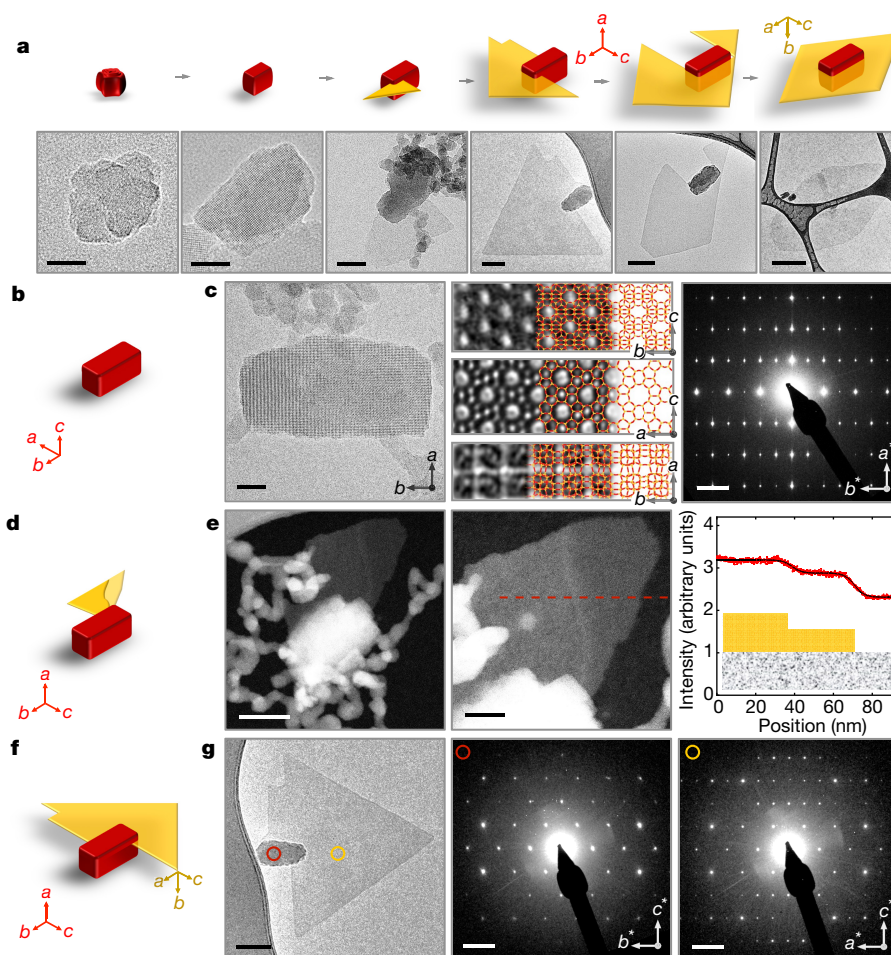


Figure 1 | Growth stages of MFI nanosheets from seed. **a**, Schematic and the corresponding bright-field TEM (BF-TEM) images, representing different stages of growth of MFI nanosheets starting from seeds approximately 30 nm in diameter. **b**, Schematic showing the preferential growth of a seed along the b axis. **c**, The corresponding TEM image of the seed in **b** (left panel); the HR-TEM images overlaid with the crystal structure model along the $[100]$, $[010]$ and $[001]$ zone axes (middle panels) confirming the MFI-type zeolite structure; and diffraction pattern of the seed taken along the $[001]$ zone axis (right panels) confirming elongation of the seed along the b axis. **d**, Schematic of a nanosheet growing out of the seed. **e**, High-angle annular dark-field scanning transmission electron microscopy (HAADF-STEM) images with different magnifications for the

seed in **d** (left and middle panels); and image intensity linescan along the red dotted line ('Position' indicates the distance from the left edge of the red dotted line) in the second HAADF-STEM image (right panel), showing a thickness step in the nanosheet that corresponds to a ratio of 5 pentasil chains to 3 pentasil chains from left to right. **f**, Schematic showing partial wrap of a b -axis-oriented nanosheet around an a -axis-oriented seed. **g**, BF-TEM image (left panel) and corresponding $[100]$ zone axis diffraction patterns (right panels) from the seed (red ring) and $[010]$ zone axis diffraction pattern from the sheet (yellow ring). Scale bars from left to right in **a** are 20 nm, 20 nm, 50 nm, 100 nm, 100 nm and 500 nm; in **c** are 20 nm and 1 nm^{-1} ; in **e** are 50 nm and 20 nm; and in **g** are 100 nm, 1 nm^{-1} and 1 nm^{-1} .

from the 30-nm seeds by epitaxial growth, and that they are not newly nucleated crystals.

After reaching this stage of growth (typically 20–40 h), a relatively rapid transition in crystal growth occurs (typically completed within a few hours). Nanosheets start to appear from one of the corners of the cylindrical crystals (approximately along the $[011]$ direction; Fig. 1d and e) and then continue to grow, encircling the seed to form a faceted nanosheet (Fig. 1a). High-angle annular dark-field (HAADF) imaging of the emerging nanosheets reveals thickness variations between their outermost portion and the part closer to the cylindrical crystal with thickness ratios of 3/4 and 3/5, which are consistent with nanosheet thicknesses of 3, 4 and 5 pentasil chains (Extended Data Fig. 3). As the nanosheet continues to grow, its thickness becomes uniform, and the nanosheet encircles the cylindrical seed and develops well defined facets (Fig. 1a, f and g and Extended Data Fig. 4). Atomic force microscopy (AFM; Fig. 2b) and electron microscopy images (Fig. 2d and e) indicate that the predominant thickness of the nanosheets upon complete encirclement of the seed is 5 nm (that is, five pentasil chains, or 2.5 unit cells thick along the b axis). With prolonged growth, the nanosheets thicken by the nucleation of islands and slow step propagation

(Extended Data Fig. 5a and b). High-resolution transmission electron microscopy (HR-TEM) imaging and simulations demonstrate that the nucleated islands are MFI and that rotational intergrowths are not present on the nanosheets (Extended Data Fig. 5c–f).

The observations described above establish a new crystal growth modality for MFI that produces the desired high-aspect-ratio nanosheet morphology. A key element of this new growth modality is the transition of the crystal growth mode from one of epitaxial slow growth on a seed crystal to one that can support the emergence and rapid growth of a nanosheet. What triggers this transition? To answer this question, we investigated the crystallographic relationship between the seed and the nanosheet. Interestingly, electron diffraction patterns (Fig. 1f and g, and Extended Data Figs 4 and 6) reveal an orthogonal rotational intergrowth relationship between them. They both share a common c axis, but their a and b axes are rotated by 90° . When we attempted to grow nanosheets starting from smaller and smoother seeds, which we prepared by disassembly of three-dimensionally ordered mesoporous-imprinted (3DOM-i) MFI crystals^{25,26}, we found a similar outcome, that is, nanosheets emerged after the 3DOM-i seeds grew to a similar cylindrical morphology (Supplementary Fig. 1). These

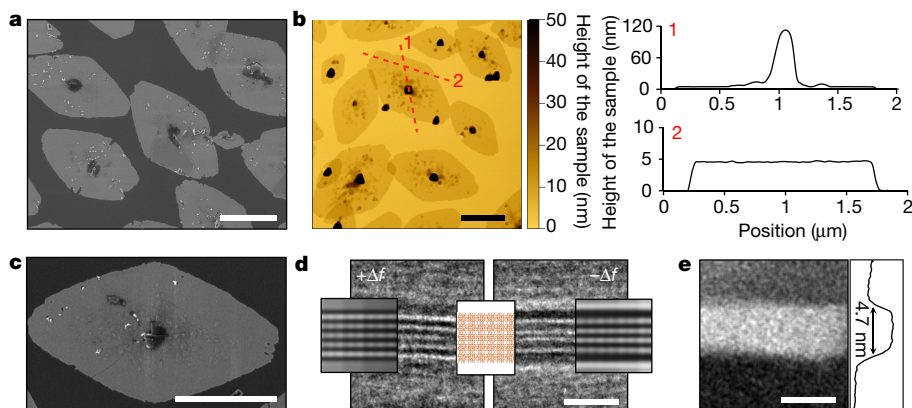


Figure 2 | Characterization of the MFI nanosheet. **a**, SEM image for MFI nanosheets. Average sizes are about $2.0\ \mu\text{m}$ and $1.2\ \mu\text{m}$ along the *a*- and *c*-axes, respectively. **b**, AFM height image and height profiles for the MFI nanosheets. The height profiles are extracted along the red dashed lines. The seed crystal at the centre is about $100\ \text{nm}$ across, and the nanosheet exhibits a very uniform thickness of $4.6 \pm 0.5\ \text{nm}$. **c**, High-magnification SEM image for the MFI nanosheet. The surface roughness of the nanosheets is due to the additional layer that forms on the top of the primary nanosheet. **d**, Underfocus ($+\Delta f$) and overfocus ($-\Delta f$) BF-TEM image with overlaid multislice simulations of a 5-pentasil-chain-thick MFI

nanosheet section along the *b*-axis. White lines in the underfocus image and black lines in the overfocus image correspond to pentasil layers in the overlaid crystal structure model. The spacing between the black and white lines is dependent on TEM imaging conditions (defocus) and is not representative of the actual bond distances between the pentasil layers. **e**, HAADF-STEM image of the nanosheet (bright area) shown in **d** with a corresponding average intensity scan confirming the thickness of the MFI nanosheet to be $4.7\ \text{nm}$ along the *b* axis. Scale bars in **a**, **b** and **c** are $1\ \mu\text{m}$ and in **d** and **e** are $5\ \text{nm}$.

results show that the emergence of nanosheets from the seeds is triggered by a single rotational intergrowth that takes place only after the seeds reach a certain size and shape. It seems that until this size and shape are attained, there are no extended flat surfaces to support the intergrowth. After the rotational intergrowth is triggered, the emerging nanosheet exposes high index (*h0l*) facets that are highly reactive and favour fast in-plane growth until a well faceted nanosheet is formed. As the facets approach the (001) and (101) faces of MFI, growth slows down. This self-regulation of in-plane growth rates allows for the final symmetric appearance of nanosheets despite their asymmetric genesis.

The proposed kinetically controlled emergence of nanosheets rather than a strain-induced transition is also supported by X-ray diffraction (XRD) data and theoretical structure optimizations. Analysis of powder XRD patterns (Extended Data Fig. 7, top) do not show substantial unit cell differences between seed crystals and nanosheets. This is in agreement with electronic structure calculations that indicate accommodation of dC5 in nearly strain-free MFI nanosheets (Extended Data Fig. 7a–f). Thermogravimetric analysis (TGA, Supplementary Fig. 2) and Ar porosimetry (Supplementary Fig. 3) show that nanosheets exhibit behaviour similar to conventional MFI.

The bottom-up seeded hydrothermal growth method developed here provides nanosheets with increased lateral dimensions and at higher yield, compared to the top-down, exfoliation-based

approaches¹⁵, allowing the facile preparation of highly oriented coatings (Supplementary Fig. 4). Moreover, their unusual 2.5-unit-cell thickness and large aspect ratio endow these nanosheets with textural properties that lie between those of conventional MFI and exfoliated MFI nanosheets and are advantageous for thin-film formation. For example, in ref. 27, the conventional MFI crystals used as seed layers for membrane formation by gel-less growth had lateral dimensions of $1.5\text{--}2.0\ \mu\text{m}$ and a thickness of about $0.5\ \mu\text{m}$, whereas the 3-nm-thick nanosheets prepared by exfoliation and used for membrane formation using a similar approach in ref. 28 had lateral dimensions that were not larger than $300\ \text{nm}$.

The dC5-MFI nanosheets reported here combine the lateral dimension of conventional MFI crystals ($1.5\text{--}2.0\ \mu\text{m}$; see Fig. 2) with nanometre-scale thickness. Moreover, because the dC5 MFI nanosheets are made by direct synthesis, they do not suffer from the fragmentation caused during exfoliation of the lamellar precursors. For these reasons, they can effectively cover porous and non-porous surfaces to create compact and oriented seed layers. Figure 3a is a top-view scanning electron microscopy (SEM) image of an MFI membrane made by gel-free secondary growth²⁷ of an oriented nanosheet deposit. It shows highly intergrown flat grains that are several micrometres in lateral dimensions. These large lateral dimensions cannot be obtained by using nanocrystalline seeds²⁹ or exfoliated nanosheets²⁸ (Extended Data Fig. 8),

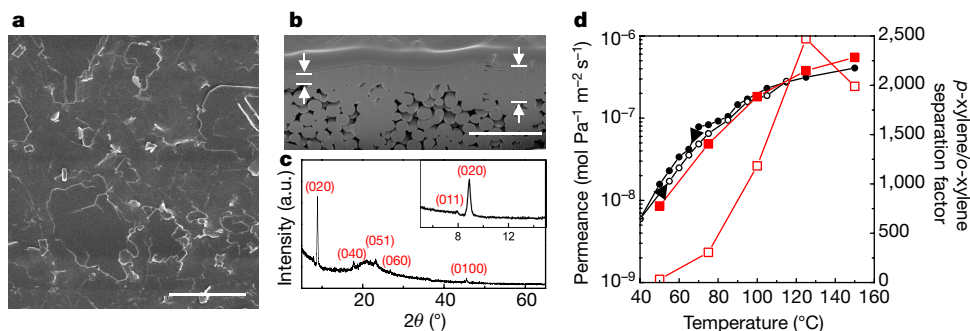


Figure 3 | Xylene separation performance for MFI membrane. **a**, **b**, Top view (**a**) and cross-sectional view (**b**) SEM images for an MFI membrane prepared by gel-free intergrowth of MFI nanosheets; scale bars represent $2\ \mu\text{m}$. **c**, XRD pattern for the MFI membrane in **a** and **b** (a.u., arbitrary units). **d**, *p*-xylene permeance and selectivity for MFI membrane: *p*-xylene

permeances from single-component permeation test measured with decreasing temperature (black circles) and increasing temperature (white circles), and *p*-xylene permeance (red squares) and separation factor (white squares) measured for a 1:1 *p*-xylene and *o*-xylene mixture. The black arrows indicate the directions of the temperature sweep.

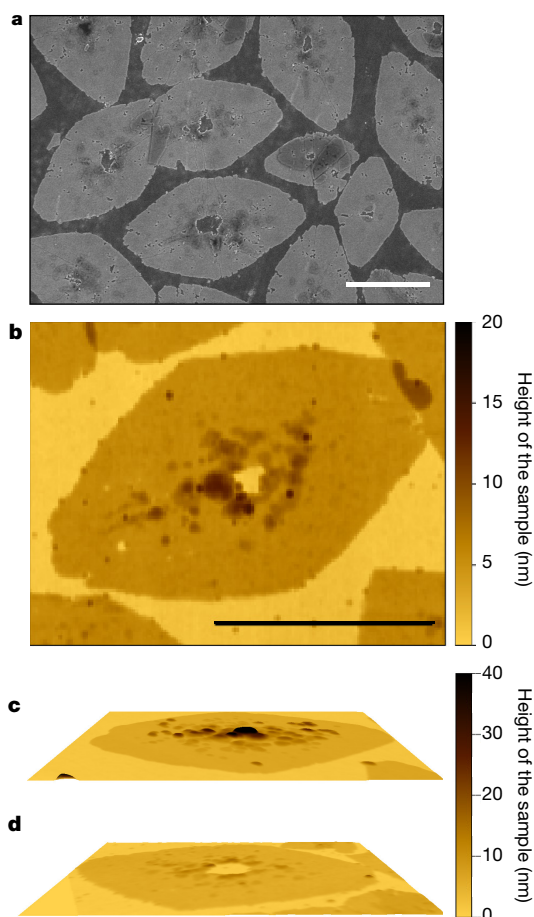


Figure 4 | Post-synthesis seed removal. **a, b**, SEM (**a**) and AFM (**b**) height images for an MFI nanosheet after seed removal by mechanical rubbing. **c, d**, AFM three-dimensional height images for an MFI nanosheet before (**c**) and after (**d**) seed removal. Both scale bars represent 1 μm .

and they are advantageous in forming films with lower density of grain boundaries, which are known to contribute to non-selective transport pathways that bypass the selective MFI micropores. Figure 3b shows an SEM cross-section establishing a dense layer after gel-free secondary growth with thickness ranging between 250 nm and 1 μm . TEM and electron diffraction investigation of the cross-sections prepared by focused ion beam reveals the presence of oriented, intergrown, and thickened nanosheets with large lateral dimensions (Extended Data Fig. 9). The few 300-nm near-rectangular crystals observed at the centres of flat grains in Fig. 3a are seed nanocrystals enlarged mostly along their *c* axis during secondary growth. They are oriented with their *a* axes perpendicular to the membrane surface. Since they occupy only a small fraction of the surface, XRD confirms that the membrane is preferentially *b*-axis out-of-plane oriented (Fig. 3c). Considering the microstructure revealed by the SEM, TEM, electron diffraction and XRD analysis presented above, we expect that molecular transport through these membranes will be dominated by the *b*-axis-oriented MFI grains formed from the nanosheets.

Indeed, the separation performance of membranes made on porous silica supports using the directly synthesized nanosheets compares favourably with membranes made by exfoliated nanosheets and also with other MFI membranes. The membrane molecular sieving properties were benchmarked using xylene isomer separation performance, which is of both practical and fundamental importance³⁰. Figure 3d shows *para*-xylene permeances and separation factors (from *ortho*-xylene) in the range 40–160 °C. Single-component permeances for *p*-xylene measured with decreasing and increasing temperature

over a period of two weeks confirmed stable and reversible membrane performance. The membrane exhibited similar high *p*-xylene permeances for single-component and binary mixtures (for example, about $0.56 \times 10^{-6} \text{ mol Pa}^{-1} \text{ m}^{-2} \text{ s}^{-1}$ at 150 °C) and very high mixture separation factors of about 2,500 at 125 °C and 2,000 at 150 °C (the next highest is about 1,000 in ref. 27). The permeance and separation factors obtained are considerably higher than those of membranes made from exfoliated nanosheets²⁸. Tests from additional membranes (Supplementary Table 1) showed that even higher separation factors (approximately 8,000) can be achieved. Although such high separation factors have not been reported before, they are anticipated by simulations³¹ (see Extended Data Fig. 10a).

Moreover, membrane performance stability was examined. Over a period of five weeks, during which the temperature of the membrane was cycled twice between 150 °C and 50 °C, the separation factor decreased from the initial value of around 2,000 to around 1,200 and the *p*-xylene permeance changed from $5.6 \times 10^{-7} \text{ mol Pa}^{-1} \text{ m}^{-2} \text{ s}^{-1}$ to $3.5 \times 10^{-7} \text{ mol Pa}^{-1} \text{ m}^{-2} \text{ s}^{-1}$ (Extended Data Fig. 10c). It is also important to note that a high separation factor was consistently observed even at low temperatures (about 300 at 75 °C and about 30 at 50 °C). At the feed conditions tested, the *p*-xylene and *o*-xylene activities at 150 °C are low, whereas at 50 °C, they are much higher (Extended Data Fig. 10c). The corresponding single-component *p*-xylene saturation loadings for free-standing MFI crystals at 150 °C and 50 °C are approximately 1 and 8 molecules per unit cell³². The increased loading is partly responsible for the large permeance drop. However, it is remarkable that high separation factors (around 30) can still be obtained under such high nominal loading conditions.

The membranes also exhibited stable performance (Extended Data Fig. 10c) and excellent *p*-xylene selectivity for multi-component mixtures of aromatics and good performance for *n*-/*i*-butane (with a separation factor of 50 at 25 °C) and alcohol/water mixtures (with a separation factor of 35 at 60 °C), as shown in Extended Data Fig. 10d and Supplementary Table 2, respectively. Although similar membrane thicknesses (<1 μm) and *p*-xylene permeance values have been reported before (Extended Data Fig. 10b), this unprecedented combination of high separation factor and high permeance for a wide range of conditions and feed mixtures can be attributed to the improved MFI membrane microstructure (thin, wide and well intergrown *b*-axis-oriented MFI grains with reduced number of grain boundary defects) enabled by the high-aspect-ratio 5-nm-thick nanosheets.

The gel-free secondary growth method^{27,28} relies on the consumption of a top sacrificial layer of 50-nm Stöber silica nanoparticles as the silica source for the growth of MFI seed layers. It is not applicable to non-silica supports like the widely used α -alumina supports. For the use of other porous supports, secondary growth methods that rely on the presence of a silica sol or gel should be employed. Recently, we reported on the use of tetraethylammonium-hydroxide silica sols to achieve homoepitaxial growth on exfoliated MFI nanosheets³³. Preliminary findings indicate that the method is applicable to dC5-MFI nanosheet seed layers (Supplementary Fig. 5) and may enable the use of MFI nanosheets for the preparation of high-quality membranes on other porous supports.

To further improve membrane performance, future efforts should be directed towards the production of high-aspect-ratio nanosheets with uniform thickness (that is, without the presence of the seed at the centre of the nanosheets). Although the ultimate approach would be based on non-seeded, non-exfoliation-based bottom-up synthesis, one way to achieve uniform thickness using the approach reported here is to attempt to remove seed crystals by chemical or mechanical means. Figure 4a and b shows SEM and AFM height images for MFI nanosheets after seed-crystal removal by rubbing. The SEM image confirms that the seed crystals were effectively removed, resulting in holes of about 50 nm across at the centre of the nanosheets. Figure 4c and d shows tilted-view AFM three-dimensional images of MFI nanosheets before and after rubbing, respectively, which confirm that the flatness

of the nanosheets is improved after rubbing. Further work in this direction will enable the large-scale implementation of ultra-thin zeolite materials in membrane separations contributing to energy-efficient separation processes.

Online Content Methods, along with any additional Extended Data display items and Source Data, are available in the online version of the paper; references unique to these sections appear only in the online paper.

Received 19 September 2016; accepted 25 January 2017.

Published online 15 March 2017.

- Flanigen, E. M. *et al.* Silicalite, a new hydrophobic crystalline silica molecular sieve. *Nature* **271**, 512–516 (1978).
- Kokotailo, G. T., Lawton, S. L., Olson, D. H. & Meier, W. M. Structure of synthetic zeolite ZSM-5. *Nature* **272**, 437–438 (1978).
- Corma, A. Inorganic solid acids and their use in acid-catalyzed hydrocarbon reactions. *Chem. Rev.* **95**, 559–614 (1995).
- Davis, M. E. Ordered porous materials for emerging applications. *Nature* **417**, 813–821 (2002).
- Cundy, C. S. & Cox, P. A. The hydrothermal synthesis of zeolites: history and development from the earliest days to the present time. *Chem. Rev.* **103**, 663–702 (2003).
- Bonilla, G. *et al.* Zeolite (MFI) crystal morphology control using organic structure-directing agents. *Chem. Mater.* **16**, 5697–5705 (2004).
- Cundy, C. S. & Cox, P. A. The hydrothermal synthesis of zeolites: precursors, intermediates and reaction mechanism. *Microporous Mesoporous Mater.* **82**, 1–78 (2005).
- Mintova, S., Gilson, J.-P. & Valtchev, V. Advances in nanosized zeolites. *Nanoscale* **5**, 6693–6703 (2013).
- Choi, M. *et al.* Stable single-unit-cell nanosheets of zeolite MFI as active and long-lived catalysts. *Nature* **461**, 246–249 (2009).
- Zhang, X. *et al.* Synthesis of self-pillared zeolite nanosheets by repetitive branching. *Science* **336**, 1684–1687 (2012).
- Mitchell, S. *et al.* Structural analysis of hierarchically organized zeolites. *Nat. Commun.* **6**, 8633 (2015).
- Roth, W. J., Nachtigall, P., Morris, R. E. & Čejka, J. Two-dimensional zeolites: current status and perspectives. *Chem. Rev.* **114**, 4807–4837 (2014).
- Díaz, U. & Corma, A. Layered zeolitic materials: an approach to designing versatile functional solids. *Dalton Trans.* **43**, 10292–10316 (2014).
- Ramos, F. S. O., de Pietre, M. K. & Pastore, H. O. Lamellar zeolites: an oxymoron? *RSC Advances* **3**, 2084–2111 (2013).
- Varoon, K. *et al.* Dispersible exfoliated zeolite nanosheets and their application as a selective membrane. *Science* **334**, 72–75 (2011).
- Zhang, H. *et al.* Open-pore two-dimensional MFI zeolite nanosheets for the fabrication of hydrocarbon-isomer-selective membranes on porous polymer supports. *Angew. Chem. Int. Ed.* **55**, 7184–7187 (2016).
- Rangnekar, N., Mittal, N., Elyassi, B., Caro, J. & Tsapatsis, M. Zeolite membranes—a review and comparison with MOFs. *Chem. Soc. Rev.* **44**, 7128–7154 (2015).
- Agrawal, K. V. *et al.* Solution-processable exfoliated zeolite nanosheets purified by density gradient centrifugation. *AIChE J.* **59**, 3458–3467 (2013).
- de Vos Burchart, E., Jansen, J. C., van de Graaf, B. & van Bekkum, H. Molecular mechanics studies on MFI-type zeolites: Part 4. Energetics of crystal growth directing agents. *Zeolites* **13**, 216–221 (1993).
- Chaikittisilp, W. *et al.* Formation of hierarchically organized zeolites by sequential intergrowth. *Angew. Chem. Int. Ed.* **52**, 3355–3359 (2013).
- Lai, Z. & Tsapatsis, M. Gas and organic vapor permeation through *b*-oriented MFI membranes. *Ind. Eng. Chem. Res.* **43**, 3000–3007 (2004).
- Khaleel, M., Wagner, A. J., Mkhoyan, K. A. & Tsapatsis, M. On the rotational intergrowth of hierarchical FAU/EMT zeolites. *Angew. Chem. Int. Ed.* **53**, 9456–9461 (2014).
- Ohsuna, T., Terasaki, O., Nakagawa, Y., Zones, S. I. & Hiraga, K. Electron microscopic study of intergrowth of MFI and MEL: crystal faults in B-MEL. *J. Phys. Chem. B* **101**, 9881–9885 (1997).
- Agger, J. R. *et al.* Silicalite crystal growth investigated by atomic force microscopy. *J. Am. Chem. Soc.* **125**, 830–839 (2003).
- Fan, W. *et al.* Hierarchical nanofabrication of microporous crystals with ordered mesoporosity. *Nat. Mater.* **7**, 984–991 (2008).
- Lee, P. S. *et al.* Sub-40 nm zeolite suspensions via disassembly of three-dimensionally ordered mesoporous-imprinted silicalite-1. *J. Am. Chem. Soc.* **133**, 493–502 (2011).
- Pham, T. C. T., Nguyen, T. H. & Yoon, K. B. Gel-free secondary growth of uniformly oriented silica MFI zeolite films and application for xylene separation. *Angew. Chem. Int. Ed.* **52**, 8693–8698 (2013).
- Agrawal, K. V. *et al.* Oriented MFI membranes by gel-less secondary growth of sub-100 nm MFI-nanosheet seed layers. *Adv. Mater.* **27**, 3243–3249 (2015).
- Yoo, W. C., Stoeger, J. A., Lee, P. S., Tsapatsis, M. & Stein, A. High-performance randomly oriented zeolite membranes using brittle seeds and rapid thermal processing. *Angew. Chem. Int. Ed.* **49**, 8699–8703 (2010).
- Sholl, D. S. & Lively, R. P. Seven chemical separations to change the world. *Nature* **532**, 435–437 (2016).
- Toda, J. *et al.* Influence of force fields on the selective diffusion of para-xylene over ortho-xylene in 10-ring zeolites. *Mol. Simul.* **41**, 1438–1448 (2015).
- Xomeritakis, G., Nair, S. & Tsapatsis, M. Transport properties of alumina-supported MFI membranes made by secondary (seeded) growth. *Microporous Mesoporous Mater.* **38**, 61–73 (2000).
- Shete, M. *et al.* Nanoscale control of homoepitaxial growth on a two-dimensional zeolite. *Angew. Chem. Int. Ed.* **56**, 535–539 (2017).

Supplementary Information is available in the online version of the paper.

Acknowledgements This work was supported by the ARPA-E programme of the US Department of Energy under Award DE-AR0000338 (0670-3240) for MFI nanosheet synthesis and characterization; by the Center for Gas Separations Relevant to Clean Energy Technologies, an Energy Frontier Research Center funded by the US Department of Energy, Office of Science, Basic Energy Sciences under Award DE-SC0001015 for membrane fabrication and permeation testing; by the US Department of Energy, Office of Basic Energy Sciences, Division of Chemical Sciences, Geosciences and Biosciences under Award DEFG02-12ER16362 for the theoretical calculations; and by the Deanship of Scientific Research at the King Abdulaziz University D-003/433 for zeolite and membrane microstructure characterization. Parts of this work were carried out in the Characterization Facility, University of Minnesota, which receives partial support from the NSF through the MRSEC programme. SEM measurements were partially performed on a Hitachi 8230 provided by NSF MRI DMR-1229263. This research used the resources of the Advanced Photon Source, a US Department of Energy (DOE) Office of Science User Facility operated for the DOE Office of Science by Argonne National Laboratory under contract number DE-AC02-06CH11357. For the theoretical calculations we used the resources of the Minnesota Supercomputing Institute and of the Argonne Leadership Computing Facility (ALCF) at Argonne National Laboratory, which is supported by the Office of Science of the Department of Energy under contract DE-AC02-06CH11357.

Author Contributions P.S.L. performed the initial experiments and with M.T. conceived the project. M.Y.J. performed extensive synthesis optimization and time-dependent growth experiments. D.K. further improved nanosheet uniformity. M.Y.J. performed the initial TEM experiments; P.K. performed all the TEM experiments described in the Letter and with K.A.M. and M.T. analysed and interpreted the data. K.N., S.N.B., S.A.-T., M.S., M.Y.J., D.K., M.T., H.S.L. and W.X. performed the XRD measurements and other microstructural characterization including TGA, Ar porosimetry, AFM and SEM and analysed and interpreted the data. M.Y.J. and D.K. fabricated the membranes. B.E. and N.R. contributed to membrane preparation. M.Y.J., D.K., N.R. and B.E. evaluated membrane separation performance. P.B., E.O.F. and J.I.S. performed and analysed the theoretical calculations. R.T. and R.F.D.J. contributed to the theoretical estimation of membrane performance. H.J.C., P.S.L. and W.F. contributed to seed synthesis. D.K., P.K., M.Y.J. and M.T. prepared the manuscript with written contributions from all co-authors. M.T. directed all aspects of the project.

Author Information Reprints and permissions information is available at www.nature.com/reprints. The authors declare no competing financial interests. Readers are welcome to comment on the online version of the paper. Correspondence and requests for materials should be addressed to M.T. (tsapa001@umn.edu), D.K. (kimx1408@umn.edu), or P.S.L. (zeolite@krcit.re.kr).

Reviewer Information *Nature* thanks J. Hedlund, J. Lin and the other anonymous reviewer(s) for their contribution to the peer review of this work.

METHODS

Chemicals. 1,5-diaminopentane (>97%), 1-iodopropane (98%), 2-butanone ($\geq 99.0\%$), potassium carbonate (anhydrous), tetrapropylammonium hydroxide (1.0 M, aqueous), sodium hydroxide (97%), potassium hydroxide (85%), silicic acid (99.9%, 20 μm), and tetraethyl orthosilicate (98%) were purchased from Sigma-Aldrich. Ethyl acetate (99.9%) and ethyl alcohol (200 proof) were purchased from Fischer Scientific. All chemicals were used as received without any further purification.

Synthesis of bis-1,5(triethyl ammonium) pentamethylene diiodide (dC5). dC5 was synthesized via exhaustive alkylation of 1,5-diaminopentane with 1-iodopropane, as reported previously⁶. In brief, 18.90 g of 1,5-diaminopentane and 82.35 g of anhydrous potassium carbonate were added to 450 ml of 2-butanone in a three-neck round-bottom flask. With a vigorous stirring, the reactor was slowly heated to 80 °C under argon atmosphere. The reactor was wrapped with aluminium foil to avoid iodide oxidation, and 108 ml of 1-iodopropane was added dropwise to the reactor. After 10 h of reaction under reflux, the reaction mixture was cooled and filtered to remove the potassium salts, and the solvent (2-butanone) in the filtrate was removed by rotary evaporation.

Purification consisted of two processes. The product was first dissolved in 250 ml of 2-butanone, and after 1 h stirring, an equal amount of ethyl acetate was added. After overnight stirring, solid powder was recovered by filtration. Additional purification was conducted with ethanol to remove KI. The recovered solid was dissolved in minimum amount of 200 proof ethanol, and then KI was removed by filtration. The product was recovered from the filtrate by using rotary evaporation. This process was repeated 4 times. The solid product was further purified with 2-butanone and ethyl acetate, followed by 200 proof ethanol, as described above. Purity was confirmed by ¹³C nuclear magnetic resonance (NMR).

Preparation of MFI seed crystals. MFI seed crystals were synthesized based on a two-stage varying-temperature synthesis³⁴ with a sol composition of 10SiO₂:2.4TPAOH:0.87NaOH:1.14H₂O³⁵. Typically, 8.93 g of 1.0 M TPAOH solution was mixed with 0.16 g of deionized water and 0.127 g of sodium hydroxide. After complete dissolution of sodium hydroxide, 2.5 g of silicic acid was added as the silica source. The mixture was stirred overnight at room temperature and then heated at 50 °C in an oil bath under static condition. After 6 days, the solution was filtered with 0.45- μm GHP (polypropylene) syringe filter, and the filtrate was heated without stirring at 100 °C in an oil bath for 3 days.

MFI seed crystals were washed with deionized water before the MFI nanosheet synthesis. The MFI crystals were collected by centrifugation at 14,500 RCF (relative centrifugal force) for 1 h followed by decantation. The solid was re-dispersed in deionized water by using ultra-sonication. After repeating the washing process twice, the solid content of the dispersion was determined based on weight after drying an aliquot of the dispersion.

MFI nanosheet synthesis. MFI nanosheets were synthesized based on the seeded growth with dC5 as SDA. Typically, a precursor sol with a composition of 80TEOS:3.75dC5:20KOH:9500H₂O was hydrolysed at room temperature under air purging (50 ml min⁻¹) to reduce ethanol content and therefore to promote MFI crystallization³⁶. After 16 h, the precursor sol was filtered with 0.45- μm GHP (polypropylene) syringe filter and then mixed with the MFI seed crystal dispersion. The silica molar ratio of the seed suspension to the dC5 precursor sol was typically 1:200 and varied between 50 and 1000. The mixture was transferred into a Teflon-lined stainless-steel autoclave and then hydrothermally treated at 140 °C under static condition. The hydrothermal treatment time was varied from 36 h to 4 d.

MFI nanosheets shown in Figs 2 and 4 were prepared using a 36 h reaction time and possessed a non-negligible amount of amorphous silica, which was removed by KOH treatment. In brief, 1 ml of as-synthesized MFI nanosheet dispersion was mixed with 1 ml of 0.1 M KOH solution and then centrifuged at 10,000 RCF for 30 s in order to remove nanosheet aggregates. Then, 1 ml of the top solution was transferred to a new centrifuge tube and diluted to 2 ml with 0.1 M KOH solution. MFI nanosheets were collected by centrifugation at 14,500 RCF for 3 min. The acquired white slurry was re-dispersed in 2 ml of 0.1 M KOH/2 M KCl solution and kept at room temperature for 8 h to dissolve amorphous silica. MFI nanosheets were then recovered by centrifugation at 14,500 RCF for 3 min and decanted. The acquired material was sequentially rinsed with 0.1 M KOH/2 M KCl solution and then 0.1 M HNO₃/2 M KCl by re-dispersion and centrifugation, as described above. The rinsing process was repeated twice with deionized water.

MFI nanosheets synthesized using a 4-day reaction time do not contain amorphous silica and were used without KOH treatment. 1 ml of as-synthesized MFI nanosheet dispersion was diluted to 2 ml with deionized water and centrifuged at 10,000 RCF for 30 s. 1 ml of the top solution was transferred to a new micro-centrifuge tube and diluted to 2 ml with deionized water. MFI nanosheets were recovered by centrifugation at 14,500 RCF for 1 min and decantation. This rinsing process with deionized water was repeated three times. The collected MFI

nanosheet slurry was then dispersed in 2 ml deionized water for characterization or 50 ml deionized water for filtration coating.

Seed removal of MFI nanosheets. MFI nanosheets were coated on Si wafer using the Langmuir–Schaefer deposition method, as reported previously³⁷. A small amount of ethanol (5 vol%) was added to freshly-prepared MFI nanosheet dispersion (2 ml, as described above), and 300 μl of the dispersion was deposited on the surface of water in polystyrene Petri dish (35-mm diameter). Si wafer was slowly lowered and contacted with the water surface to transfer the MFI nanosheets to the Si wafer. Then, the Si wafer was tilted and lifted upward, and water remaining on the Si wafer was removed by air blow. Prepared MFI nanosheet coating was then calcined at 400 °C for 6 h at a ramp rate of 1 °C min⁻¹. MFI nanosheets on Si wafer were then rubbed by cotton fabric to detach the seeds, followed by additional calcination under identical conditions to remove any organic contamination.

MFI membrane fabrication. MFI membrane was fabricated on porous silica support based on inter-growth of MFI nanosheets. Sintered silica fibre (SSF) supports were prepared from quartz fibre and Stober silica, as previously reported²⁸. 1 g of freshly prepared (50 ml, as described above) MFI nanosheet dispersion was then coated on SSF supports with the vacuum-assisted filtration method^{15,28}. During the filtration coating, vacuum was maintained above 10 psi to keep the filtration slow. The filtration was typically finished within 2 h and kept under vacuum overnight for complete drying. The MFI nanosheet coatings on SSF supports were calcined at 400 °C for 6 h at a ramp rate of 1 °C min⁻¹ under 100 ml min⁻¹ of air flow after each coating step. Filtration coating was repeated until no vacancy was observed by SEM analysis.

Continuous MFI membranes were prepared by gel-free growth of MFI nanosheets on SSF supports²⁷. In brief, nanosheet-coated SSF supports were impregnated with 0.025 M TPAOH solution and placed in a Teflon-lined stainless-steel autoclave after excess solution on the side and bottom of the support was removed by Kimwipes. The autoclave was then heated at 180 °C for 2 d. The resultant membrane was rinsed with deionized water and dried at 70 °C. Before xylene isomer vapour permeance measurements, the membrane was calcined at 450 °C for 8 h at a ramp rate of 1 °C min⁻¹.

Characterization. TGA was conducted using a Shimadzu TGA-50 analyser. Samples were dried at 120 °C for 8 h under nitrogen atmosphere, and TGA profiles were recorded in air flow (100 ml min⁻¹) with a ramp rate of 1 °C min⁻¹. Argon porosimetry was performed at 87 K by using Quantachrome AutosorbIQ MP. Prior to measurements, the samples were outgassed and heated at 573 K for 16 h under vacuum. The samples were analysed for adsorption and desorption ranged from 10⁻⁷ to 1 of P/P₀. SEM images were recorded by using a Hitachi SU 8230 or Hitachi S-4700 operated at 1.5 kV. High-resolution SEM images were acquired in a deceleration mode of Hitachi SU 8230 with 0.8-kV landing voltage. Height profiles of calcined MFI nanosheets on Si wafers were acquired in a tapping mode under ambient condition by using Bruker Nanoscope V Multimode 8. Focused-ion-beam milling was performed with a FEI Quanta 200 3D, in order to make a trench on the membrane for cross-sectional measurements. XRD patterns of MFI membranes were recorded by using a PANalytical X'Pert Pro diffractometer with Cu K α radiation. High-resolution powder diffraction data were collected at beamline 17-BM of the Advanced Photon Source with a monochromatic beam of 0.72768 Å at Argonne National Laboratory. Powder samples were prepared by freeze-drying with the Labconco FreeZone 4.5 l Benchtop Freeze-Dry System. Collected data were processed with GSAS II³⁸ and converted to 2 θ values corresponding to Cu K α radiation. Pawley fitting was employed to extract lattice parameters using GSAS II. The in-plane XRD measurements were performed at beamline 33-BM-C at the Advanced Photon Source (0.8267 Å), Argonne National Laboratory. The instrumentation consists of a bending magnet source with a Si(111) monochromator with a 0.9 \times 0.5 mm beam spot. The sample was placed on a Huber 4-circle stage with the sample held almost parallel to the incident beam, and the detector was moved in the plane of the sample. 2 θ values were then converted to those corresponding to Cu K α radiation.

Conventional TEM was performed on a FEI Tecnai G2 F30 (S)TEM with TWIN pole piece, a Schottky field-emission electron gun operating at 300 kV and equipped with a Gatan 4k \times 4k Ultrascan CCD. Imaging and diffraction data collection were performed under low electron dose to minimize electron beam damage of the zeolite sample. HAADF-STEM images were acquired in an aberration-corrected FEI Titan 60-300 (S)TEM, operating at 200 kV and having a STEM incident probe convergence angle of 24 mrad with 20 pA screen current and about 50 mrad HAADF detector inner angle. MFI nanosheet samples were prepared for TEM measurement by drop-casting an aqueous suspension of the MFI nanosheets on TEM grids (ultrathin carbon film on holey carbon support film, 400 mesh Cu, Ted Pella). The grid was dried at room temperature before imaging in the TEM. An electron transparent TEM sample of the membrane cross-section was prepared by focused-ion-beam milling using a FEI Quanta 200 3D instrument. The sample

was first coated with a platinum layer about 5 μm thick, and polishing of the cross-section was performed using a 10-pA focused ion beam to minimize damage to the membrane by the ion beam.

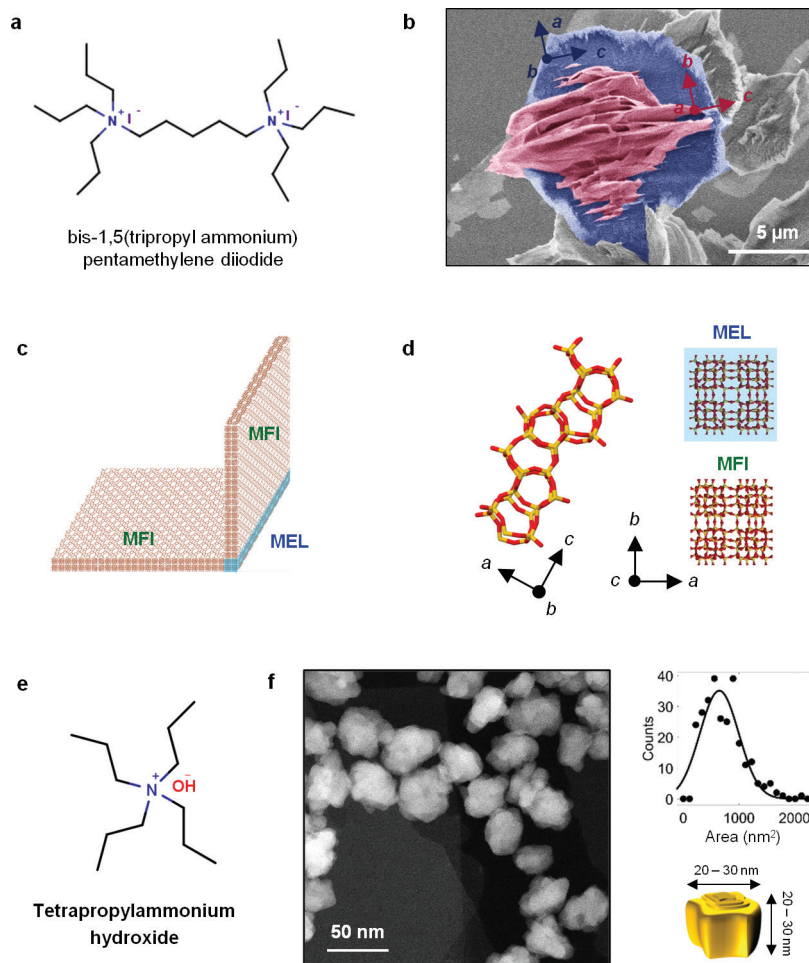
Theoretical calculations. The model membrane system consists of $1 \times 3 \times 1$ unit cells of the MFI structure, with periodic replication in the a axis and c axis directions and the two $\{010\}$ surfaces truncated, and 1–6 dC5 cations. The exposed oxygen atoms were terminated as surface silanol groups, and 30 Å vacuum space was added to the b -axis direction. To maintain charge neutrality of the system, an appropriate number of deprotonated silanol defects (SiO^-) was created to compensate for the SDA cations. Periodic Kohn–Sham density functional theory calculations were performed using the Vienna *Ab initio* Simulation Package, version 5.4.1³⁹, with the PBE exchange–correlation functional⁴⁰, Grimme D2 dispersion corrections⁴¹, the valence electron density expanded in a plane-wave basis set using a kinetic energy cutoff of 400 eV, and the core electrons described by the projected-augmented wave method³⁹. Sampling of the unit cell was carried out at the Γ -point. During the geometry optimizations, the cell shape was allowed to change but the total volume was kept constant. The vacuum space present in the supercell permits the MFI membrane to swell or contract freely.

To estimate the ratio of self-diffusion coefficients along the straight channel for the p -xylene/ o -xylene pair, first principles (FP) and force-field-based (FF) molecular dynamics simulations (using CP2K, version 3.0⁴², and GROMACS, version 2016.1⁴³) in the canonical ensemble in conjunction with umbrella sampling and weighted histogram analysis methods⁴⁴ were carried out. The FP molecular dynamics simulations considered a 3-nm MFI nanosheet (1.5 unit cells terminated by silanol groups) and used the PBE exchange–correlation functional⁴⁰ and Grimme D3 dispersion correction⁴⁵. The FF molecular dynamics simulations probed a bulk MFI sample (represented by a periodic simulation box consisting of $2 \times 2 \times 3$ unit cells), and the TraPPE force field was used to describe xylene–xylene and xylene–zeolite interactions with harmonic potentials allowing for flexibility of sorbate and framework⁴⁶.

Membrane testing. Xylene isomer vapour permeance measurements were conducted in the Wicke–Kallenbach mode, in which total pressures of feed and permeate are maintained at atmospheric pressure⁴⁷. Feed comprises approximately equimolar mixture of p -xylene (about 0.5 kPa) and o -xylene (about 0.5 kPa), and helium was used as a carrier and sweep gas. The compositions of feed and permeate were assessed with a gas chromatograph (Agilent, 7890B) equipped with a flame ionization detector and a capillary column (DB-WAXetr, Chrometech). The permeance is defined as the flux divided by the partial pressure gradient. The separation factor is defined as the molar ratio of isomers in the permeate divided by the molar ratio of isomers in the feed. The separation performances of identically prepared membranes were also evaluated for the n - i -butane mixture²⁸ and the ethanol/water mixture⁴⁸, as reported previously.

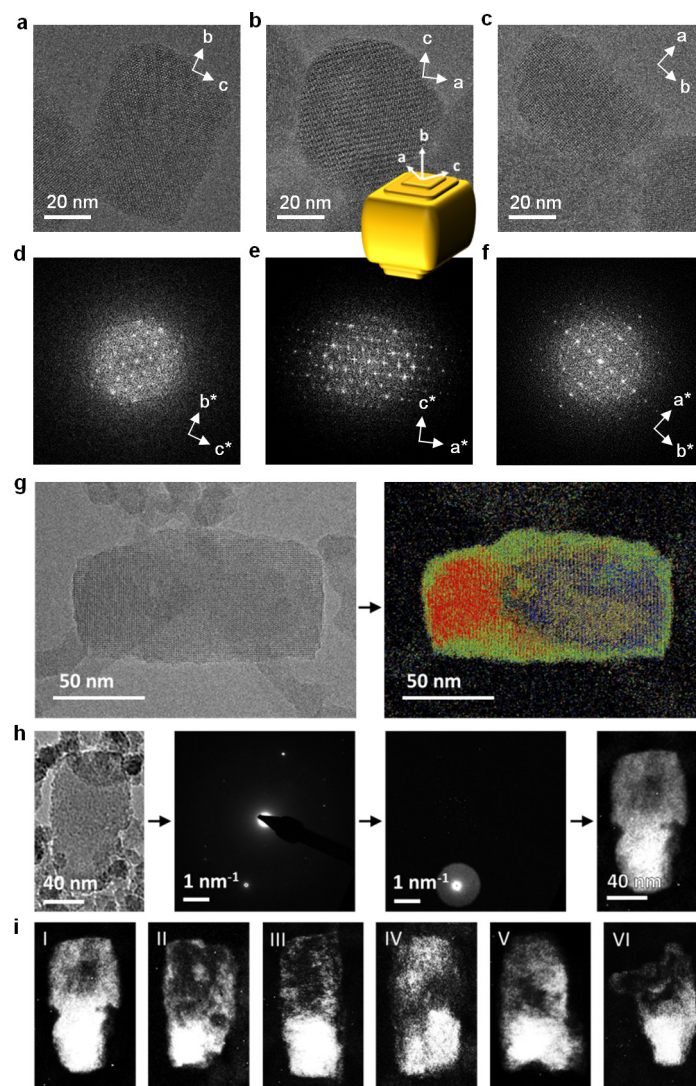
Data availability. The data sets generated during and/or analysed during the current study are available from the corresponding author on reasonable request.

34. Li, Q., Creaser, D. & Sterte, J. The nucleation period for TPA-silicalite-1 crystallization determined by a two-stage varying-temperature synthesis. *Microporous Mesoporous Mater.* **31**, 141–150 (1999).
35. de Moor, P.-P. E. A., Beelen, T. P. M. & van Santen, R. A. In situ observation of nucleation and crystal growth in zeolite synthesis. A small-angle X-ray scattering investigation on Si-TPA-MFI. *J. Phys. Chem. B* **103**, 1639–1650 (1999).
36. Cheng, C. H. & Shantz, D. F. Silicalite-1 growth from clear solution: effect of alcohol identity and content on growth kinetics. *J. Phys. Chem. B* **109**, 19116–19125 (2005).
37. Rangnekar, N. *et al.* 2D zeolite coatings: Langmuir–Schaefer deposition of 3 nm thick MFI zeolite nanosheets. *Angew. Chem. Int. Ed.* **54**, 6571–6575 (2015).
38. Toby, B. H. & Von Dreele, R. B. GSAS-II: The genesis of a modern open-source all purpose crystallography software package. *J. Appl. Cryst.* **46**, 544–549 (2013).
39. Kresse, G. & Joubert, D. From ultrasoft pseudopotentials to the projector augmented-wave method. *Phys. Rev. B* **59**, 1758–1775 (1999).
40. Perdew, J. P., Burke, K. & Ernzerhof, M. Generalized gradient approximation made simple. *Phys. Rev. Lett.* **77**, 3865–3868 (1996); erratum *Phys. Rev. Lett.* **78**, 1396 (1997).
41. Grimme, S. Semiempirical GGA-type density functional constructed with a long-range dispersion correction. *J. Comput. Chem.* **27**, 1787–1799 (2006).
42. Hutter, J., Iannuzzi, M., Schiffrin, F. & VandeVondele, J. cp2k: atomistic simulations of condensed matter systems. *Wiley Interdiscip. Rev. Comput. Mol. Sci.* **4**, 15–25 (2014).
43. Van Der Spoel, D. *et al.* GROMACS: fast, flexible, and free. *J. Comput. Chem.* **26**, 1701–18 (2005).
44. Grossfield, A. WHAM: The weighted histogram analysis method. Version 2.0.9. <http://membrane.urmc.rochester.edu/content/wham> (2013).
45. Grimme, S., Antony, J., Ehrlich, S. & Krieg, H. A consistent and accurate ab initio parametrization of density functional dispersion correction (DFT-D) for the 94 elements H–Pu. *J. Chem. Phys.* **132**, 154104 (2010).
46. Vlugt, T. J. H. & Schenk, M. Influence of framework flexibility on the adsorption properties of hydrocarbons in the zeolite silicalite. *J. Phys. Chem. B* **106**, 12757–12763 (2002).
47. Choi, J., Ghosh, S., King, L. & Tsapatsis, M. MFI zeolite membranes from a - and randomly oriented monolayers. *Adsorption* **12**, 339–360 (2006).
48. Elyassi, B. *et al.* Ethanol/water mixture pervaporation performance of b -oriented silicalite-1 membranes made by gel-free secondary growth. *AIChE J.* **62**, 556–563 (2016).
49. Keizer, K., Burggraaf, A. J., Vroon, Z. A. E. P. & Verweij, H. Two component permeation through thin zeolite MFI membranes. *J. Membr. Sci.* **147**, 159–172 (1998).
50. Xomeritakis, G., Lai, Z. & Tsapatsis, M. Separation of xylene isomer vapors with oriented MFI membranes made by seeded growth. *Ind. Eng. Chem. Res.* **40**, 544–552 (2001).
51. Hedlund, J. *et al.* High-flux MFI membranes. *Microporous Mesoporous Mater.* **52**, 179–189 (2002).
52. Lai, Z. *et al.* Microstructural optimization of a zeolite membrane for organic vapor separation. *Science* **300**, 456–460 (2003).
53. Choi, J. *et al.* Grain boundary defect elimination in a zeolite membrane by rapid thermal processing. *Science* **325**, 590–593 (2009).



Extended Data Figure 1 | Structure of dC5 SDA and corresponding MFI/MEL intergrowth, and structure of TPAOH SDA and corresponding TPA-MFI seeds. **a**, Structure of bis-1,5(tripropyl ammonium) pentamethylene diiodide (dC5). **b**, An SEM image of non-seeded growth of MFI nanosheets conducted with a precursor composition identical to that used for seeded nanosheet growth and a reaction time of 12 days. **c**, Schematic illustration of twinning via MFI/MEL intergrowth.

d, Structure of pentasil chain and projections of MEL and MFI structures along the c axes (yellow and red represent silicon and oxygen atoms, respectively). **e**, Structure of tetrapropylammonium hydroxide. **f**, HAADF-STEM image of MFI seed crystals with a distribution of projected areas (right top) and a schematic illustration of the crystal (right bottom). The average linear dimension of crystals, based on the projected area, is calculated to be about 30 nm.



Extended Data Figure 2 | Crystallographic orientation and internal structure of TPA MFI seeds after secondary growth with dC5 (before nanosheet initiation). a–f, BF-TEM images and the corresponding fast Fourier transforms of a seed after secondary growth with dC5 along the [100] direction (a, d); the [010] direction (b, e); and the [001] direction (c, f). Overlaid in yellow is the schematic of the seed crystal after secondary growth with dC5, where the longest dimension is along the *b* axis or [010] direction. g, High-resolution BF-TEM image (left panel) of grown seed (before the emergence of nanosheet) shown in Fig. 1c along the *c* axis. The coloured image (right panel) corresponds to a digitally processed HR-TEM image using a Sobel filter, followed by thresholding and binary colouring to highlight different fringe patterns in the

HR-TEM image. Similarly coloured regions correspond to areas with the same crystallographic orientation/thickness. h, Demonstration of the procedure for obtaining dark-field images of the grown seeds. A BF-TEM image of a seed and its corresponding diffraction pattern are acquired. The bright diffraction spot is selected by placing the objective aperture in the diffraction plane. The dark-field TEM image formed using the selected spot shows domains of different crystallographic orientation/thickness within the seed as seen in g. i, Different seeds (before the emergence of nanosheets) imaged in dark-field mode using the method shown in h reveal regions of different crystallographic orientation/thickness within the seed.

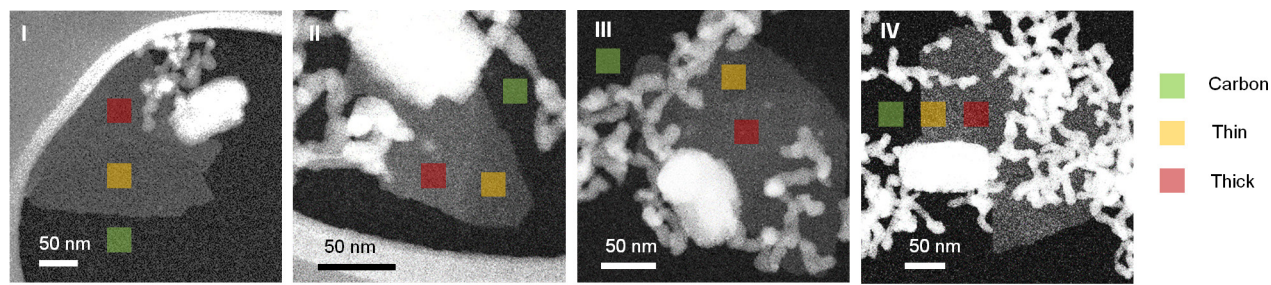
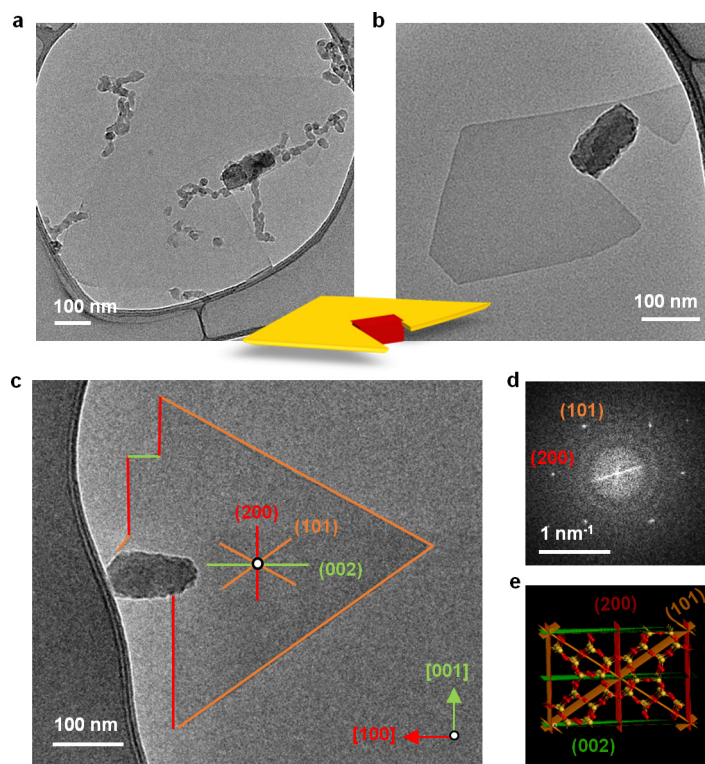


Image	I_{carbon}	I_{Thin}	I_{Thick}	$\frac{I_{thick} - I_{carbon}}{I_{thin} - I_{carbon}}$	Pentasil chains (p.c.)
I	3.08	3.28	3.32	1.20	$\frac{5 \text{ p.c.}}{4 \text{ p.c.}} = 1.25$
II	2.36	2.86	3.19	1.66	$\frac{5 \text{ p.c.}}{3 \text{ p.c.}} = 1.67$
III	3.36	3.88	4.16	1.54	$\frac{5 \text{ p.c.}}{3 \text{ p.c.}} = 1.67$
IV	3.19	3.51	3.58	1.22	$\frac{5 \text{ p.c.}}{4 \text{ p.c.}} = 1.25$

Extended Data Figure 3 | Thickness variation in nucleated nanosheet. Panels I–IV show HAADF-STEM images of partially grown sheet from the seed. Marked in green, yellow and red are the carbon background, and the thin and thick regions of the nanosheet, respectively. The average intensity

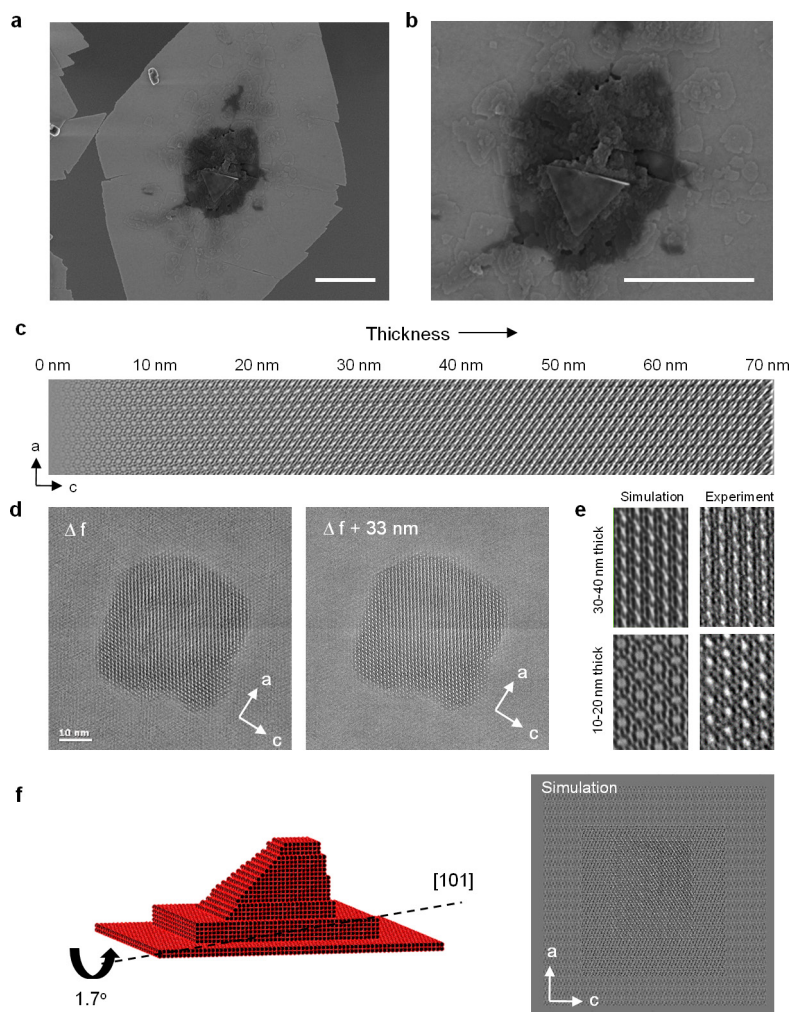
of these marked regions is tabulated. The ratio of intensity from the thick and thin regions after carbon background (from carbon support of the TEM grid) subtraction matches the corresponding ratio of either 5/4 or 5/3 pentasil chains.



Extended Data Figure 4 | Partial wrap of sheets around seeds.

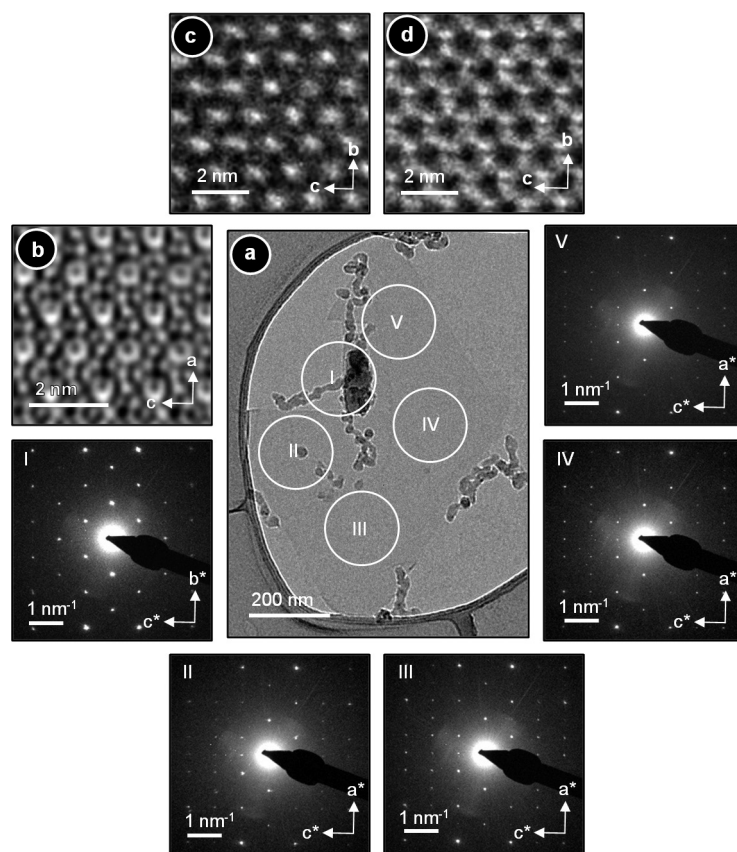
a, b, Two representative BF-TEM images of partial wraparound of sheets around seeds. The thicker seeds appear darker and the thinner large-area nanosheets appear lighter. Overlaid is a schematic of the partial wraparound of the sheet (yellow) around the seed (red). **c,** BF-TEM image of partial wrap of *b*-axis-oriented sheet around the *a*-axis-oriented seed shown in Fig. 1g. The edges of the growing diamond-shaped sheet are

terminated by (101) crystallographic planes. Overlaid in colour are the crystallographic planes forming different faces of the nanosheet. **d,** Fast Fourier transform of HR-TEM image of the sheet in **c**, confirming the crystallographic directions marked in **c**. **e,** Unit cell of the MFI crystal illustrating the atomic connectivity of planes forming the edges of the sheet shown in **c**.



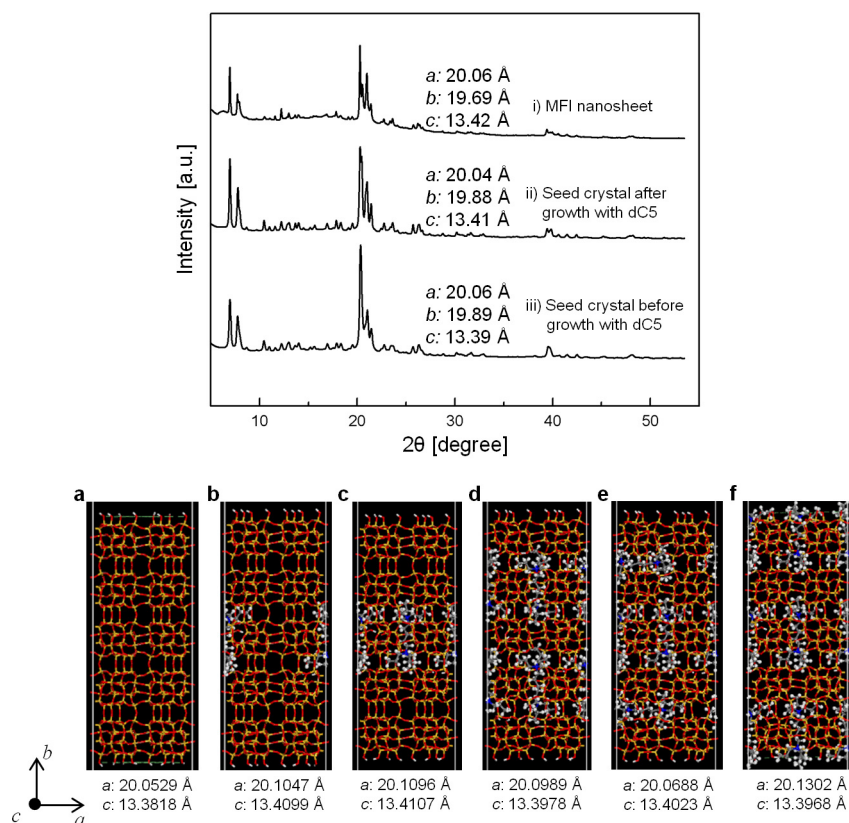
Extended Data Figure 5 | Thickening of MFI nanosheets by epitaxial island nucleation. **a, b**, SEM images of MFI nanosheets synthesized at 140 °C for 4 days. Additional layers formed continuously on top of the primary nanosheet, resulting in thickening of the central part. The darker contrast at the centre is attributed to charging caused by absence of good contact with support. Both scale bars represent 500 nm. **c**, Multislice simulated BF-TEM image (accelerating voltage $V_0 = 300$ kV, spherical aberration coefficient $C_s = 2$ mm, defocus $df = 100$ nm) of MFI crystal with increasing thickness (left to right) in the b -axis direction. The MFI crystal shown here has a slight mis-tilt (1.7° about the $[101]$ axis) from the $[010]$ zone axis to match experimental imaging conditions. The effect of a small mis-tilt is amplified in the HR-TEM image owing to an increase in thickness from left to right. Regions with 0–10 nm thickness demonstrate a typical $[010]$ zone axis pattern while those of 20–70 nm

thickness exhibit complex HR-TEM image patterns. **d**, BF-TEM images of a thick island growing epitaxially on top of the nanosheet. Images taken at defocus Δf and $\Delta f + 33$ nm represent imaging conditions with the nanosheet in focus (note the clear appearance of the MFI structure in the background) and the thick island in focus, respectively. **e**, Comparison of two different image sections, one taken from within the thick island HR-TEM image in **d** and the other from multislice simulations in **c**, shows the presence of regions with thickness 10–40 nm varying along the b -axis direction. **f**, Model of a thick island with steps 6–10 nm in height along the b -direction on a 5-nm-thick nanosheet. The corresponding multislice simulation ($V_0 = 300$ kV, $C_s = 2$ mm, $df = 100$ nm) of the MFI crystal model shows a HR-TEM pattern similar to those observed in **d**, thus confirming the epitaxial growth of thick regions on a thin MFI nanosheet.



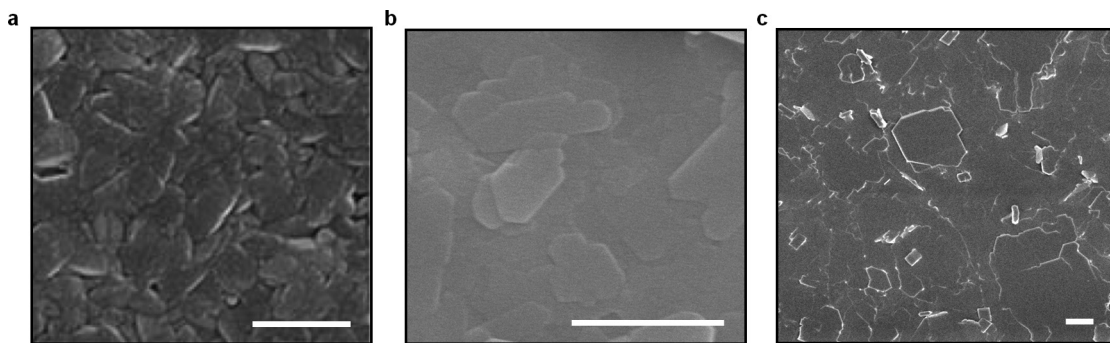
Extended Data Figure 6 | Crystallographic relationship between seed and nanosheet orientation. **a**, BF-TEM imaging of partial wrap of nanosheet around the seed. The white circle marked as region (I) encloses the seed, and the corresponding diffraction pattern confirms the orientation of the seed along the a axis. Regions marked as (II), (III), (IV) and (V) enclose the nanosheet and the corresponding diffraction

patterns confirm the b -axis orientation of the nanosheet. **b**, Bragg-filtered HR-TEM image of the MFI nanosheet showing the typical $[010]$ zone-axis pattern. **c**, **d**, HR-TEM images of the seed oriented along $[100]$ zone-axis taken at under-focus (**c**) and over-focus (**d**) imaging conditions. The data support the idea that the seed and sheet are connected by an a/b twin crystallographic relationship.



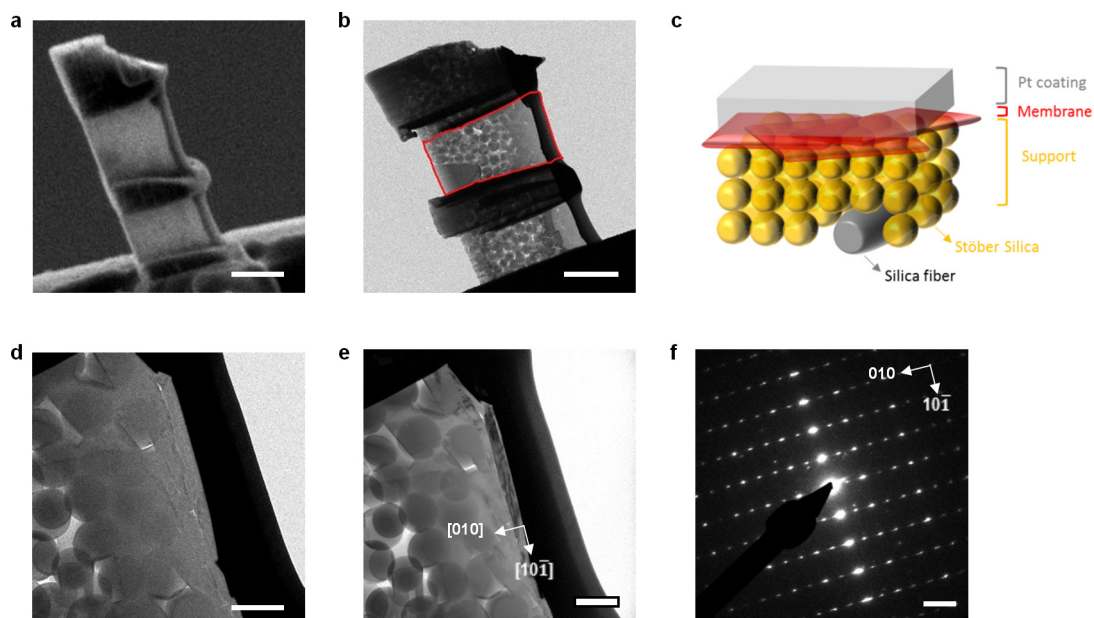
Extended Data Figure 7 | Powder XRD data and analysis (top), and electronic structure calculation (bottom) for strain in dC5 MFI nanosheets. XRD patterns for the MFI nanosheet (i) and seed crystals after (ii) and before (iii) growth with dC5. The initial seed crystal (iii) was prepared with TPAOH, resulting in a conventional MFI structure. Seed crystals after growth with dC5 (ii) and MFI nanosheets (i) exhibit *a*- and *c*-axis lattice parameters comparable to those of the seed crystal (iii), which indicates that dC5 yields non-strained MFI materials (at the resolution of the current experiment). **a–f**, Model MFI/SDA systems obtained from density functional theory calculations. The membrane framework consists of $1 \times 3 \times 1$ unit cells of the MFI structure, with the two {010} surfaces truncated and 30 \AA of vacuum space (not shown in figure) added to the *b*-axis direction. The empty framework (**a**) therefore contains five layers of pentasil chains. In addition, up to six dC5 SDA cations per simulation cell were considered: one (**b**) or two (**c**) dC5 molecules located in the straight channels and sandwiching the centre pentasil layer; four dC5 molecules, either all located in the straight channels sandwiching the second and

fourth pentasil layers (**d**), or with two in the straight channels and the other two in the zigzag channels (**e**); and six dC5 molecules saturating the straight channels with four of them partially extending beyond the outer surfaces (**f**). Geometry optimizations were performed first using an empirical force field and then via density functional theory calculations. The branching sites in dC5 molecules can only be accommodated at channel intersections, whose centre-to-centre separations are about 10 \AA , while the distance between the two N atoms of dC5 is roughly 7.6 \AA in the all-*trans* conformation of the pentamethylene chain. Despite this incompatibility of length scales and the substantial amount of strain present in adsorbed SDA molecules, relatively minor energetic differences were found for the arrangement of SDA molecules in the straight versus zigzag channels; for example, **e** is higher in energy than **d** by less than $0.2 \text{ kJ per mole of SiO}_2$ units. Furthermore, the strain affects SDA molecules more than the inorganic framework itself, and consequently, the *a* and *c* lattice parameters lengthen by only 0.1% – 0.4% , while the *b* lattice parameter shrinks by only 0.02% – 0.24% .



Extended Data Figure 8 | Grain-size comparison of MFI membranes prepared from different seeds. a–c, SEM top-view images for MFI membranes prepared by secondary growth of MFI nanocrystals (a), exfoliation-based MFI nanosheets (b), and dC5 MFI nanosheets (c).

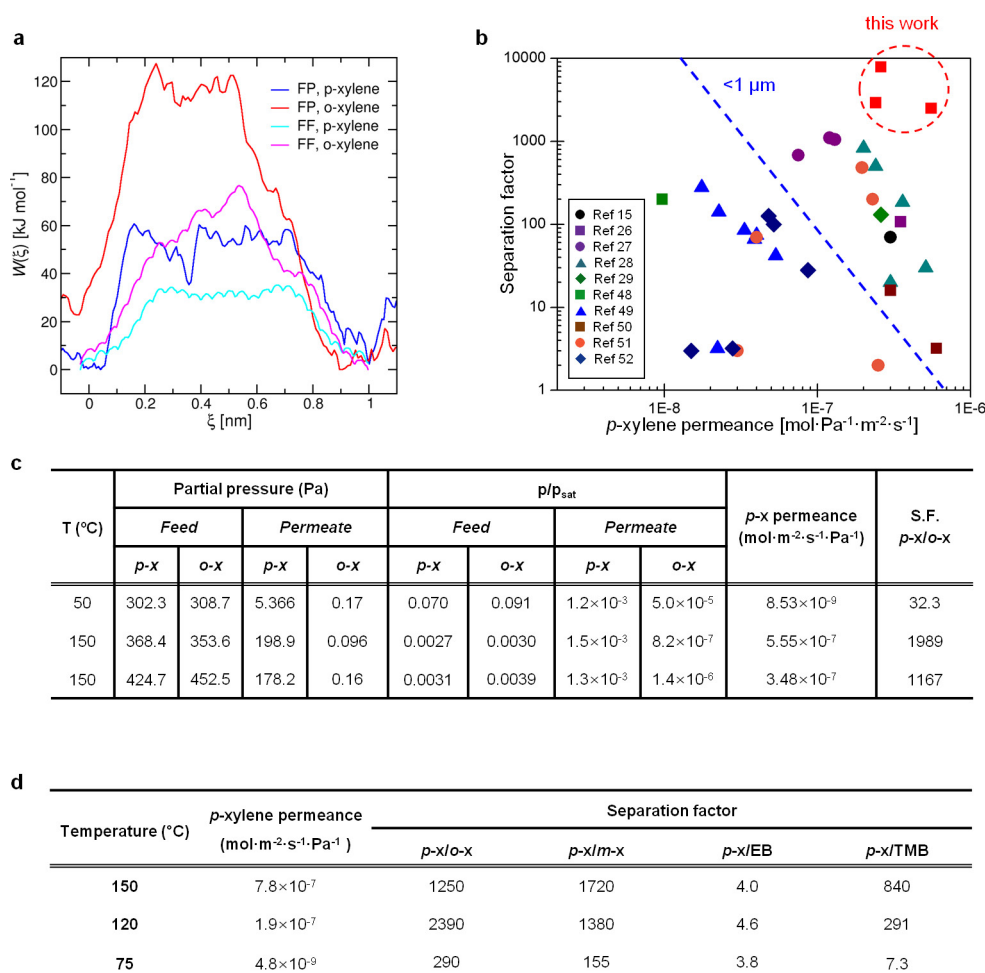
Lateral dimensions of MFI grains of the membrane fabricated from dC5 MFI nanosheets are much larger than those fabricated from MFI nanocrystals and exfoliation-based MFI nanosheets. All scale bars indicate 500 nm.



Extended Data Figure 9 | TEM and electron diffraction of MFI nanosheet membrane after gel-free secondary growth.

a, b, Low-magnification SEM (**a**) and BF-TEM images (**b**) of focused-ion-beam milled section. **c**, Schematic of the area highlighted in red in **b**. The spherical particles are Stöber silica particles coated onto the porous support. The edge of a silica fibre from the main body of the porous support is also visible. The intergrown membrane layer does not exceed

1 μm . **d**, High-magnification BF-TEM image of highlighted area shown in **b**. Plate-like intergrown grains with thickness of 100–200 nm form a top layer of about 200 nm, followed by a less intergrown deposit that penetrates the Stöber silica layer. **e, f**, BF-TEM image (**e**) of highlighted area shown in **b** tilted near to the $\langle 101 \rangle$ zone axis of a nanosheet grain with the corresponding electron diffraction pattern (**f**). Scale bars in **a** and **b** are 2 μm , in **d** and **e** are 400 nm and in **f** is 1 nm^{-1} .



Extended Data Figure 10 | Xylene isomer separation performance.

a, Potentials of mean force for p -xylene and o -xylene along the straight channel, $W(\xi)$, were obtained from FP molecular dynamics simulations for a 3-nm MFI film at $T = 573$ K and from FF molecular dynamics simulations for bulk MFI at $T = 423$ K. Based on the potentials of mean force, the p -xylene/ o -xylene self-diffusion coefficient ratios are estimated as 1.2×10^4 (FF molecular dynamics; $\Delta W \approx 33$ kJ mol $^{-1}$) and 4×10^4 (FP molecular dynamics; $\Delta W \approx 50$ kJ mol $^{-1}$). FF-based Monte Carlo simulations for bulk MFI and 5-nm film indicate that adsorption of o -xylene is slightly favoured, but the adsorption selectivity is less than 2 at low loading. **b**, Comparison of p -xylene/ o -xylene separation performances of the membrane reported here and other reports. Thin ($< 1 \mu\text{m}$) MFI membranes have been reported to exhibit high permeances^{15,26–29,49–53}, and our membranes show remarkable combinations of high permeances and high separation factors (S.F.), which were enabled by use of high-aspect-ratio dC5 MFI nanosheets (1–2 μm lateral dimensions and 5 nm

thicknesses) as seeds. **c**, Representative permeation data with p - and o -xylene partial pressures in feed and permeate. Feed is an approximately equimolar mixture of p - and o -xylene in a carrier gas (helium), and permeate is a stream composed of p -xylene and o -xylene passing through the membrane and a carrier gas (helium). The second 150 °C measurement was performed after 39 days of testing (from when the first 150 °C measurement was performed). Tests in between these two measurements included single (p -xylene), binary (p - and o -xylene) and multicomponent (p -, o -, m -xylene, TMB, EB mixture) measurements and temperature cycling from 150 °C to about 50 °C twice. p/p_{sat} was calculated using p_{sat} for p -x: 4,328 Pa at 50 °C and 136,424 Pa at 150 °C and for o -x: 3,375 Pa at 50 °C and 116,768 Pa at 150 °C; p_{sat} is the saturated vapour pressure. **d**, p -xylene separation performance measured for a multi-component mixture (p -x: p -xylene, o -x: o -xylene, m -x: m -xylene, EB: ethylbenzene, TMB: trimethylbenzene).